Demyelination reduces brain parenchymal stiffness quantified in vivo by magnetic resonance elastography

Katharina Schregel[a,b,1], Eva Wuerfel née Tysiak[c,1], Philippe Garteiser[b], Ines Gemeinhardt[d], Timour Prozorovski[e], Orhan Aktas[e], Hartmut Merz[f], Dirk Petersen[a], Jens Wuerfel[a,g,2,3], and Ralph Sinkus[b,2]

[a]Institute of Neuroradiology, University Luebeck, 23568 Luebeck, Germany; [b]Université Paris Diderot, Sorbonne Paris Cité, CRB3, UMR 773, Inserm, F-92110 Clichy, France; [c]Department of Pediatrics, University Luebeck, 23568 Luebeck, Germany; [d]Institute of Radiology, Charité - University Medicine Berlin, 10117 Berlin, Germany; [e]Department of Neurology, University Medical Center Duesseldorf, Heinrich-Heine-University, 40225 Duesseldorf, Germany; [f]Department of Pathology, University Luebeck, 23568 Luebeck, Germany; and [g]NeuroCure Clinical Research Center, Charité - University Medicine Berlin, 10117 Berlin, Germany

Edited by Michael Sela, Weizmann Institute of Science, Rehovot, Israel, and approved March 6, 2012 (received for review January 23, 2012)

The detection of pathological tissue alterations by manual palpation is a simple but essential diagnostic tool, which has been applied by physicians since the beginnings of medicine. Recently, the virtual "palpation" of the brain has become feasible using magnetic resonance elastography, which quantifies biomechanical properties of the brain parenchyma by analyzing the propagation of externally elicited shear waves. However, the precise molecular and cellular patterns underlying changes of viscoelasticity measured by magnetic resonance elastography have not been investigated up to date. We assessed changes of viscoelasticity in a murine model of multiple sclerosis, inducing reversible demyelination by feeding the copper chelator cuprizone, and correlated our results with detailed histological analyses, comprising myelination, extracellular matrix alterations, immune cell infiltration and axonal damage. We show firstly that the magnitude of the complex shear modulus decreases with progressive demyelination and global extracellular matrix degradation, secondly that the loss modulus decreases faster than the dynamic modulus during the destruction of the corpus callosum, and finally that those processes are reversible after remyelination.

magnetic resonance imaging | elasticity imaging | tissue integrity

Palpation of the brain, a hands-on experience long exclusive to neurosurgeons and pathologists detecting brain pathology, has recently become a domain for physicists and radiologists: Using magnetic resonance elastography (MRE), it is possible today to noninvasively assess the biomechanical properties of brain parenchyma in vivo. In MRE, viscoelasticity describes the tendency of tissue to resist deformation, thus translating the subjective tactile information gained from palpation into a quantifiable objective measure. These properties can be acquired by analyzing the propagation of low-frequency shear waves, which are mechanically elicited in an organ of interest (1, 2).

Recent preliminary studies described distinct viscoelastic characteristics of the brain parenchyma in healthy subjects as well as changes by aging and brain pathology, underlining the applicability and relevance of cerebral MRE (3, 4). During physiological aging, there was evidence for a brain parenchymal "liquification" reflected in the decrease of solid-fluid behavior of the tissue (5). In patients suffering from multiple sclerosis (MS), a significant decrease of cerebral viscoelasticity was noted already in early disease stages compared with healthy controls (6).

However, despite a rising collection of in vivo viscoelasticity data, no study has yet directly correlated viscoelastic parameters assessed via MRE with histopathological analyses. Thus, the question on how in vivo mechanical properties translate into cellular and molecular conditions has remained open.

Magnetic resonance imaging (MRI) has emerged as most important paraclinical tool for the diagnosis and monitoring of neuroinflammatory diseases like MS, as reflected by current diagnostic criteria (7). Nevertheless, disease specificity of conventional MRI parameters such as T2 lesion load is limited and their association with clinical course and neurological disability is only modest (8). Additionally, these conventional MRI parameters provide only limited conclusions to be drawn with respect to the underlying pathology of MS lesions. Novel in vivo parameters are necessary that are capable of evaluating demyelination and repair, and thus may improve diagnostic specificity and predictive value in MS.

Therefore, we assessed brain parenchymal viscoelasticitiy noninvasively by MRE in a mouse model of reversible toxic demyelination, and correlated our findings to detailed histological analyses. The copper chelator cuprizone was used as demyelination model and fed to susceptible mouse strains (C57BL/6 mice) resulting in progressive demyelination in several brain regions, particularly in the corpus callosum (9–11). We show in this particular model that the degree and the time kinetics of the induced disruption of extra-axonal tissue integrity (i.e., extensive demyelination and distinctive extracellular matrix (ECM) degradation) lead to a decrease of viscoelasticity in the corpus callosum. The biomechanical changes of the corpus callosum detected in this animal model are consistent with previously published human data, showing a global decrease of brain parenchymal viscoelasticity in MS patients (6).

Results

Viscoelasticity Images of Brain Tissue. MRE maps of cerebral tissue viscoelasticity generate an easily interpretable graphic image of the underlying brain anatomy, identifying the corpus callosum significantly stiffer than all other structures (Fig. 1). As expected, ventricles exhibited low shear properties. A decrease of viscoelasticity within the corpus callosum after 12 wk of cuprizone feeding was clearly visible.

Physiological Development of MRI and MRE Parameters During Adolescence. Initially, we studied physiological changes of MRI and MRE parameters during adolescence in a group of 5- to 6-wk-old healthy female C57BL/6 mice. The corpus callosum showed a significant progressive decrease in T2 signal intensity during the observation period in this group (Fig. 2*A*, white bars). Interestingly, the mechanical phase angle y remained constant over time (Fig. 2*B*, white bars), whereas viscoelasticity expressed

Author contributions: E.W.n.T., J.W., and R.S. designed research; K.S., T.P., J.W., and R.S. performed research; P.G., I.G., D.P., and R.S. contributed new reagents/analytic tools; K.S., E.W.n.T., P.G., I.G., T.P., H.M., J.W., and R.S. analyzed data; and K.S., E.W.n.T., P.G., O.A., J.W., and R.S. wrote the paper.

The authors declare no conflict of interest.

This article is a PNAS Direct Submission.

[1]K.S. and E.W.n.T. contributed equally to this work.

[2]J.W. and R.S. contributed equally to this work.

[3]To whom correspondence should be addressed. E-mail: jens.wuerfel@charite.de.

This article contains supporting information online at www.pnas.org/lookup/suppl/doi:10.1073/pnas.1200151109/-/DCSupplemental.

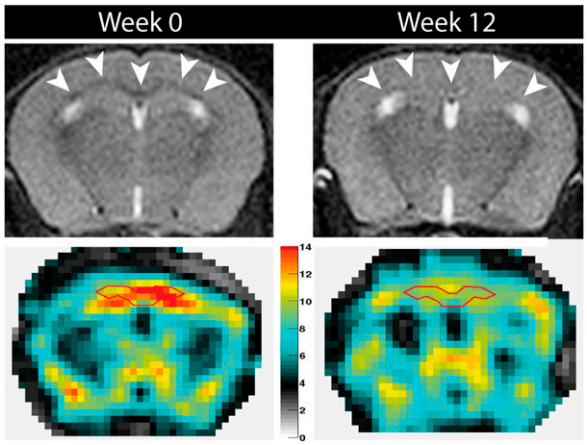

Fig. 1. T2-weighted MRI (above) and reconstructed maps of the complex-valued shear modulus $|G^*|$ (below). (*Left*) A healthy control. (*Right*) A mouse after 12 wk of continuous cuprizone diet. During treatment, the T2 signal intensity of the myelinated corpus callosum (arrowheads) became isointense to the neighboring gray matter, and viscoelasticity showed a significant decrease in the region-of-interest (marked by the red line), corresponding to progressive demyelination.

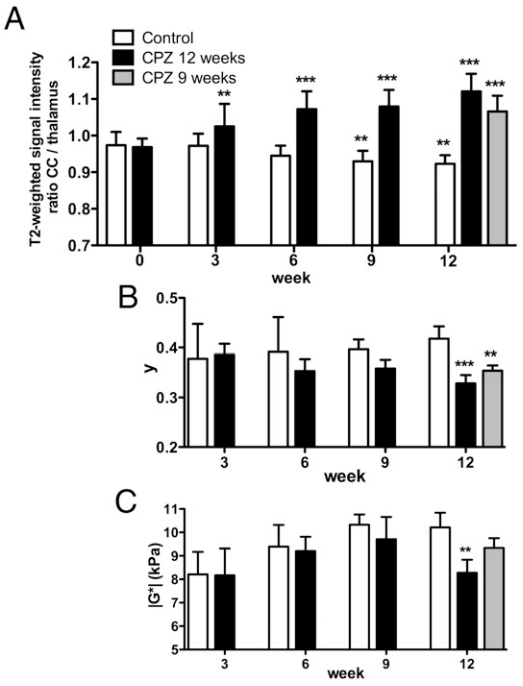

Fig. 2. Quantitative analysis of T2-weighted signal intensity (*A*), phase-angle *y* (*B*) and viscoelasticity $|G^*|$ (*C*) in the corpus callosum. Longitudinal data in healthy control mice (HC; white bars), cuprizone-fed mice (CUP; black bars), and mice discontinuing cuprizone diet after 9 wk (gray bars) are presented. (*A*) T2-weighted signal intensity was computed as ROI ratio of corpus callosum and thalami. This ratio developed reciprocally in HC and CUP: Although, initially, the two groups did not differ (week 0), T2-signal intensity decreased significantly in HC ($P < 0.0001$), but increased progressively in CUP, reaching a maximum at week 12. (*B*) Whereas *y* was constant in HC, it decreased progressively in CUP, reaching a minimum in week 12. (*C*) Viscoelasticity rose in HC and CUP between weeks 3 and 9; however, this increase was less pronounced in CUP. $|G^*|$ reached a plateau in HC, but decreased significantly in CUP at week 12. Mice returning to normal diet at week 9 partially recuperated. $^{**}P < 0.001$, $^{***}P < 0.0001$; treated mice compared with HC in Bonferroni-corrected one- or two-way ANOVA at every time point (in consequence, α was lowered and results were classified as significant when *P* value was < 0.025). SD by whiskers.

by $|G^*|$ initially increased by ~20%, and subsequently stabilized ($P = 0.0009$) (Fig. 2*C*, white bars).

Cuprizone-Induced Alterations of MRI and MRE Parameters. We further assessed whether the dynamic changes of MRI and MRE parameters during physiological maturation are influenced by toxic demyelination induced by feeding 0.2% cuprizone to a second group of animals for a period of 12 wk. These mice developed a signal increase of the corpus callosum up to gray matter isointensity on T2-weighted imaging, beginning at week 3 (Fig. 2*A*, black bars). In MRE, the parameter *y* constantly decreased during cuprizone feeding reciprocally to the alterations detected on T2-weighted signal intensity. This decrease was most pronounced at week 12 (Fig. 2*B*, black bars). On the other hand, changes of $|G^*|$ followed a different time course: This parameter rose from week 3 to week 9, analogous to the alterations observed in the healthy control group; however, the degree of change was less pronounced. Interestingly, at week 12, we noted a significant decrease of $|G^*|$ in the cuprizone-fed mice ($P < 0.01$) (Fig. 2*C*, black bars).

A third group of mice discontinued the cuprizone diet after week 9 and was followed-up with normal chow. In this cohort, cuprizone induced changes in T2-weighted signal intensity, *y* as well as $|G^*|$ were all partially reversible at week 12 (Fig. 2, gray bars).

Cuprizone-Induced Demyelination and ECM Alterations. We assessed de- and remyelination in immunohistochemical stainings against myelin basic protein (MBP) and additionally applying the fluorescent marker fluoromyelin. Control mice did not show any significant changes of myelination over time.

Demyelination of the corpus callosum of cuprizone mice was initially apparent after 3 wk of cuprizone feeding and constantly progressed during the entire observation period of 12 wk. In those mice halting cuprizone diet after 9 wk, slight remyelination was noticed at 12 wk (Fig. 3).

Furthermore, we conducted detailed analyses of ECM composition and longitudinal alterations applying hematoxylin and eosin (H&E) staining, Alcian blue staining and immunohistochemical stainings for fibronectin (Fig. 4) and neurocan.

In the cuprizone cohort, we noted an increase of the overall cell density within the corpus callosum in H&E staining, starting within 3 wk after initiation of the cuprizone diet. The cell density was highest at week 6. Simultaneously, the composition of the ECM appeared less dense and lost homogeneity: The number of parenchymal vacuoles increased and eosinophilia vanished (Fig. 4*A*, *Top*). In Alcian blue staining, we observed a significant upregulation of glycosaminoglycans and mucopolysaccharides of the callosal ECM beginning at week 3 (Fig. 4*A*, *Middle*). The expression of fibronectin increased during cuprizone-feeding, reaching a maximum after 12 wk of cuprizone diet (Fig. 4*A*, *Bottom*). The evaluation of the neurocan staining remained ambiguous: We found a highly heterogenous neurocan expression in individual mice, but not a distinct pattern differentiating the study groups. The transient expression of neurocan underlies complex dynamic processes in physiological as well as inflammatory conditions that may even result in coexistent up- and down-regulation nearby (12).

Remarkably, all forecited stainings showed significant macroscopically visible transformations of the ECM: The overall matrix composition became highly heterogenous. In some areas, the tissue density clearly thinned up to loss of parenchyma, accompanied by progressive vacuolization. In other patches, we noted an increase of matrix substance due to enhanced depositioning of ECM molecules (glycosaminoglycans, mucopolysaccharides) and proteins such as fibronectin. We semiquantitatively assessed this

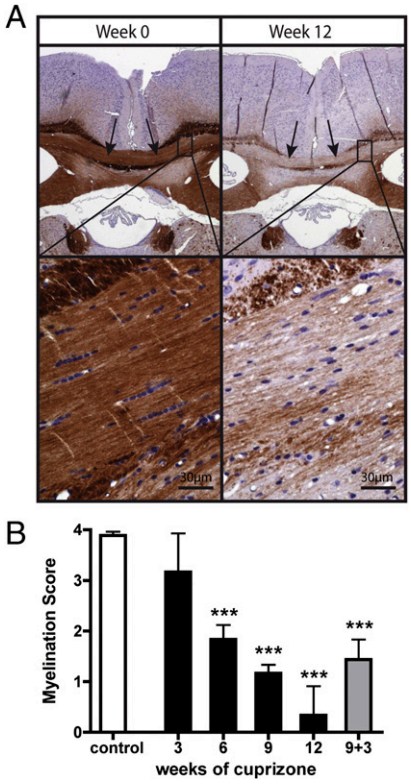

Fig. 3. To assess demyelination, brain sections were immunohistochemically stained for myelin basic protein (MBP). (*A*) Overview and magnification of the corpus callosum (arrows) in a healthy control (HC; left side) and a mouse after 12 wk on cuprizone diet (CUP; right side). HC stained homogeneously with intact myelin sheaths. In contrast, CUP at week 12 showed almost complete demyelination. (*B*) Semiquantitative analysis of demyelination with scores ranging from 4 = normal myelination, to 0 = no myelin. Pooled data of HC are given (white bar). In CUP, demyelination progressed constantly and was almost complete after 12 wk of cuprizone feeding (black bars). The subgroup of mice returning to normal chow after 9 wk of cuprizone diet showed incomplete remyelination at week 12 (gray bar). ***$P < 0.0001$; CUP compared with HC in an unpaired *t* test at every time point (in consequence, α was lowered and results were classified as significant when *P* value was < 0.01). SD by whiskers.

process, applying an "ECM score" (Fig. 4*B*, see also *SI Materials and Methods*), which linearly increased during cuprizone feeding.

In summary, ECM alterations and demyelination followed a comparable time course. Cuprizone withdrawal at week 9 induced a reversal of the ECM alterations described above.

Immune Cell Infiltration and Activation Due to Cuprizone Feeding. We further assessed the infiltration and activation of immune cells in the corpus callosum during cuprizone feeding to investigate cell-based factors influencing the parenchymal viscoelasticity. Immunofluorescent and/or conventional immunohistochemical stainings were accomplished for T lymphocytes, macrophages/microglia and astrocytes. In healthy control mice, we noted the presence of a small number of resident macrophages/microglia and astrocytes, which did not perceptibly change during the time course of the experiment.

In the cuprizone cohort, an early immigration of a small number CD3+ T cells into the corpus callosum was observed, which was most pronounced 3 wk after initiating the cuprizone diet (Fig. S1). The number of IBA-1-expressing macrophages/microglia largely increased within the corpus callosum starting at 3 wk, peaking after 9 wk, and declining again at 12 wk of cuprizone diet (Fig. S2). Astrogliosis, marked by GFAP staining, coincided with the kinetics of macrophage immigration/microglial activation, however, with a delayed start at 6 wk (Fig. 5). In summary, the immune cell infiltration into the corpus callosum of cuprizone-fed mice followed a different time course compared with the changes of MRE parameters, reaching a maximum at week 9, and declining in all investigated cell types thereafter.

In the subgroup of mice discontinuing with the cuprizone diet after week 9, we could not detect any effect on immune cell presence compared with the cuprizone group at week 12.

Influence of Cuprizone Feeding on Axons. We also investigated the effect of cuprizone on neurons, because changes of axonal integrity might influence viscoelastic properties of the corpus callosum. Immunofluorescent stainings were performed for β-amyloid precursor protein (β-APP). Minimal background β-APP staining was observed in control mice. In cuprizone mice, there was a significant increase of the β-APP expression in ovoid-like axonal structures, which reached a maximum at 9 wk and slightly declined at week 12 (Fig. 6). To assess whether the observed increase of β-APP expression in cuprizone mice implied axonal damage, we additionally stained for different neurofilament markers (phosphorylated neurofilaments H and M, detected by SMI-31 and SMI-34 antibodies). No differences could be observed between healthy controls and cuprizone mice, and no changes were detectable during the whole course of the experiment.

Discussion

MRE has recently become applicable to study biomechanical alterations of the brain under physiological and pathological conditions. Evidence of significant changes of viscoelastic properties in CNS diseases such as MS (6) or normal pressure hydrocephalus (3) affirm the potential of MRE to fill a diagnostic gap, providing the opportunity for a noninvasive, quantifiable palpation of brain parenchyma. Particularly in neuroinflammatory diseases, where MRI has emerged as most important parameter for diagnosis and treatment monitoring, despite weak disease specificity and prognostic value, more specific disease parameters are necessary. Here, we demonstrate how changes of brain stiffness measured by MRE translate into alterations on a cellular and molecular level. Our data indicate that biomechanical properties of the brain parenchyma are modified during brain maturation processes in physiological conditions. Toxic demyelination in the cuprizone model significantly altered parenchymal biomechanical properties. These findings can be used to interpret the loss of brain viscoelasticity in patients suffering, e.g., from MS, as reported (6).

In adolescent healthy mice, the mechanical phase angle y remained constant whereas the viscoelasticity $|G^*|$ in the corpus callosum increased during the time course of the experiment, reaching a plateau after 9 wk of observation, corresponding to 14 wk of age. Concurrently, the T2-weighted signal intensity in the corpus callosum decreased over time. These changes in $|G^*|$ and T2-weighted signal intensity may be interpreted as evidence of ongoing brain maturation during adolescence. The development of the cerebral architecture including cell division and migration, axonal and dendritic sprouting and sorting-out, as well as final myelination of fiber tracts continues in humans and rodents after birth (13). In a recent MRI study using diffusion tensor imaging, fiber maturation of the corpus callosum reached a plateau ~30–40 d after birth (14). The global biochemical composition of the brain parenchyma was shown to largely change during the first 60 d after birth with an increase of proteolipid protein and myelin basic protein (MBP), peaking at 10–18 d of age (15). Assuming similar kinetics of the myelin synthesis in our murine model, large-scale myelination would have been completed at the beginning of the experiment. This is in line with our own histological analyses, which do not show any dynamics of myelin staining in healthy mice. Contrarily and in accordance to the literature, alterations of the ECM continue up to adulthood,

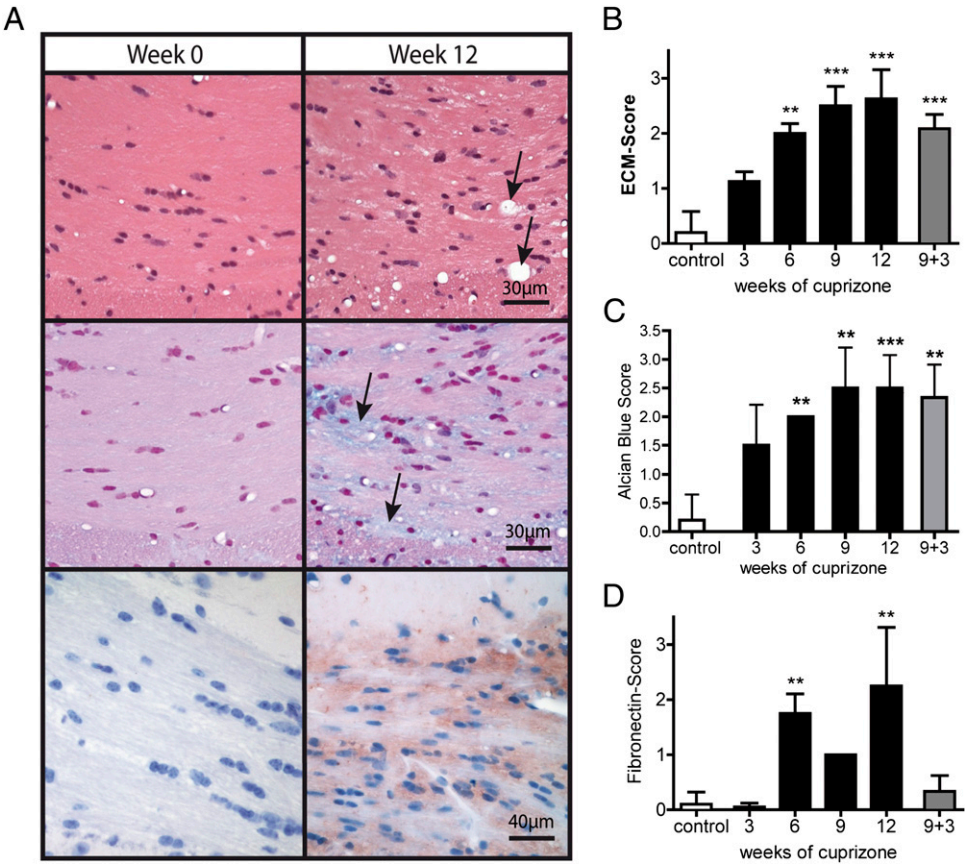

Fig. 4. (*A*) Extracellular matrix (ECM) alterations were studied by hematoxylin and eosin (H&E, *Top*), Alcian blue (AB, *Middle*), and immunohistochemical fibronectin (FN) stainings (*Bottom*). The corpus callosum of healthy controls (HC; *Left*) was homogenous and showed an intact tissue structure on all stainings. AB (glycosaminoglycans, mucopolysaccharides) and FN were barely present in the corpus callosum of HC. In contrast, the parenchyma of mice after 12 wk on cuprizone diet (CUP; *Right*) was markedly altered. H&E depicted a heterogeneously composed ECM with vacuoles (arrows; *Top Right*) and eosinophilia. AB showed a patchy accumulations of glycosaminoglycans and mucopolysaccharides (blue staining, arrows; *Middle Right*). FN staining in the corpus callosum increased largely (brown staining; *Bottom Right*). An increasing cell density was evident in all stainings after cuprizone feeding. (*B*) Tissue integrity alterations were assessed applying a semiquantitative score in H&E, AB and FN staining. The score ranged from 0 (normal) to 3 (heavily altered ECM; vacuoles, disruption). Controls (white bar) were pooled. In CUP (black bars), alterations were constantly progressive and reached a maximum at week 12. In mice discontinuing the cuprizone diet after 9 wk (gray bar), ECM recuperated incompletely. The extent of AB (*C*) and FN (*D*) staining in the corpus callosum was evaluated with a score ranging from 0 (no staining) to 3 (intense staining). Controls (white bar) were pooled. In CUP (black bars), stainings were most pronounced after 12 wk of cuprizone diet. $^{**}P < 0.001$, $^{***}P < 0.0001$; CUP compared with HC with an one-way ANOVA. SD by whiskers.

reflected by a decrease of the ECM volume fraction from 40% at birth to 20% at adulthood (16). We hypothesize that the increase and stabilization of $|G^*|$ in healthy adolescent mice observed in our study may be attributed to physiological brain maturation, in particular reorganization processes of the ECM. Interestingly, an inverse development showing the decrement of cerebral viscoelasticity was recently shown during physiological aging in a human study (5); however, this has not been investigated on a cellular or molecular level so far.

In cuprizone-fed mice, we noted two different kinetics regarding the temporal evolution of MRE parameters: firstly, the phase angle y continuously decreased between week 3 and week 12, paralleling the increase in T2-weighted relative signal intensity; secondly, we measured a smaller increase of $|G^*|$ compared with control mice until week 9 of the experiment, and subsequently a significant loss of $|G^*|$ at week 12, which was less pronounced in the subcohort halting cuprizone diet. We compared the kinetics of these biomechanical parameters with cellular and molecular histological analyses to identify the underlying pathophysiology causing the observed changes in mechanical properties:

Axonal or extra-axonal processes? Axons are important players constituting the biomechanical properties of brain tissue because they penetrate the parenchyma, forming a stabilizing grid-like structure. Also, neurons were shown to be significantly stiffer than glial cells in an in vitro assessment of biomechanical properties of single cells (17). Inconsistent data have been published regarding the influence of cuprizone on the neuronal cell population. Lindner et al. described an enhanced β-APP immunoreactivity, which peaked at 4–6 wk of cuprizone feeding, which was judged as minimal acute axonal damage. Chronic axonal degeneration detected by SMI-32 staining was first seen after 8 wk and peaked after 16 wk of cuprizone feeding (18). Other studies report only a marginal or transient influence of cuprizone on neurons and axonal integrity (19, 20). In our study, increased β-APP was noted predominantly in ovoid-like axonal structures peaking after 9 wk of cuprizone feeding, suggesting a failure of fast axonal transport. Such findings indicate either axonal damage or abnormal intracellular β-APP-transport (21, 22). To distinguish between these, we performed staining for phosphoneurofilaments H and M, SMI-31 and SMI-34, which showed no evidence of neurodegeneration. Thus, the transient increase of β-APP expression rather depicts impeded axonal transport, possibly due to mitochondrial failure. In our experimental set-up, the significant reduction of viscoelasticity in the corpus callosum occurred at week 12 and was hence not correlated with the

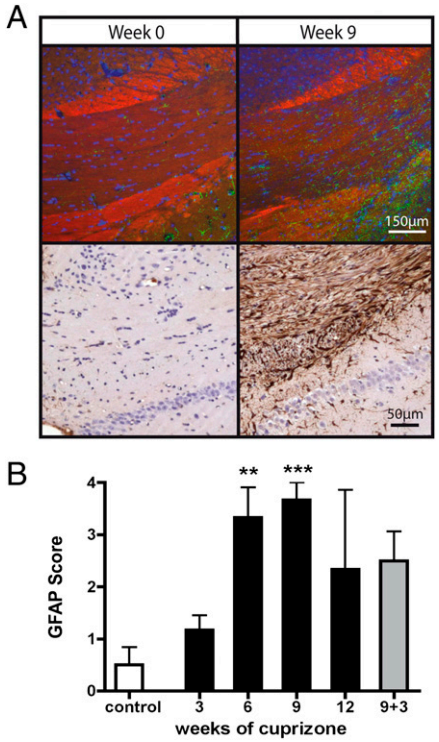

Fig. 5. Astrogliosis was assessed by immunohistochemical staining for glial fibrillary acidic protein (GFAP). (*A*) Extensive astrogliosis was observed after 9 wk of cuprizone feeding (*Right*; *Upper*: green = GFAP, astrocytes; blue = Hoechst 33258, cell nuclei; red = fluoromyelin; *Lower*: gliosis, brown in DAB staining) in comparison with control mice (HC; *Left*). (*B*) Semiquantitative analysis of gliosis in the corpus callosum. The score ranges from 0 (none) to 4 (massive gliosis); HC were pooled (white bar). In treated mice (black bars), astrogliosis increased progressively until reaching a maximum at week 9, and declined thereafter. $^{**}P < 0.001$, $^{***}P < 0.0001$; treated mice compared with HC in an unpaired *t* test at every time point (in consequence, α was lowered and results were classified as significant when *P* value was < 0.01). SD by whiskers.

increased β-APP expression and is therefore probably independent from neurons and axons.

Demyelination and ECM alterations? Demyelination could be clearly shown in MBP and fluoromyelin stainings. The loss of myelin continuously increased until week 12. The linear progression of the demyelination correlated closely with the reduction of the phase angle *y* and was also reflected by a drop of relative T2-weighted signal intensity in cuprizone mice. Moreover, alterations of the structural integrity of the ECM paralleled the time courses of demyelination and *y*. Whereas in our study the T2-weighted signal intensity was additionally altered by continuous brain maturation, changes of *y* could be solely assigned to demyelination and ECM degradation, because *y* did not change in the control group. Thus, both the parameter *y* and T2-weighted signal changes are sensitive to the degree of structural integrity, but only *y* is specific to these.

The parenchymal integrity of the corpus callosum in cuprizone-fed mice was largely altered. We observed a progressive disaggregation of the ECM with the formation of vacuoles as well as vanishing of brain parenchyma on one hand, and a patchy accumulation of fibronectin, glycosaminoglycans, and mucopolysaccharides on the other hand, the later assumably caused by local inflammatory processes. A similar up-regulation of ECM molecules has been reported in MS and other inflammatory CNS diseases (12, 23–25). However, we were not able to identify a single and unique ECM component causing the cuprizone effect on viscoelastic properties alone. This is not surprising: The current state of knowledge assigns a functional role to ECM molecules in the CNS (directing maturation, degeneration, and repair processes) more than keeping a simple structural/mechanical role (23, 26). The local up-regulation of several ECM proteins during cuprizone feeding, as we show, might contribute to the degree of structural dysintegrity within the corpus callosum, additionally to the vacuolization and loss of parenchyma. The combination of such disturbances in a highly structured matrix composition might cause the severe drop in $|G^*|$ observed at the late time point of 12 wk cuprizone feeding (27).

Inflammatory processes? We studied the kinetics of immune cell migration to the corpus callosum, to investigate a possible influence on brain parenchymal biomechanics because inflammation has been suspected to alter tissue stiffness in liver MRE (28). Specifically, a model of acute inflammation in rat liver demonstrated a steep increase in viscoelasticity (29), as expected from normal clinical experience. There is general agreement that parenchymal alterations during cuprizone feeding are not immune mediated despite the fact that the migration of T cells to the brain of cuprizone-treated animals has been reported (20, 30, 31). The time course of astrogliosis, infiltration, and activation of macrophages/microglia in our study was in line with data published by other groups (9, 18, 30, 31); cellular inflammation peaked at an early time point, markedly before the significant reduction of *y* and the drop in viscoelasticity. Therefore, a decrease in viscoelasticity is unlikely to be caused by local accumulation of immune cells directly, but rather by inflammation-dependent alterations of the ECM.

Reviewing its biphasic course, we assume that two competing mechanisms influence $|G^*|$ in cuprizone mice: On one hand,

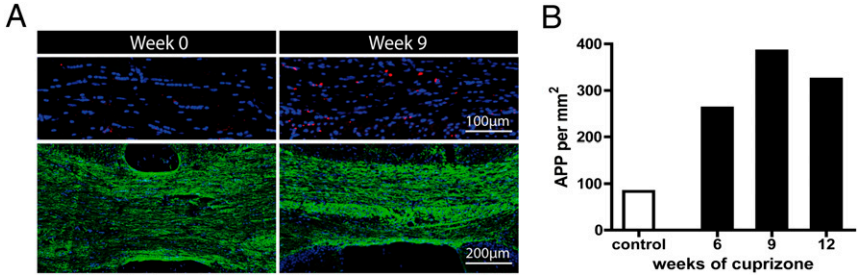

Fig. 6. Cuprizone feeding did not induce permanent neuronal damage. (*A*) The expression of β-amyloid precursor protein (β-APP) was transiently increased after 9 wk of cuprizone feeding compared with control mice (*A Upper*: red = β-APP; blue = Hoechst dye 33258, cell nuclei). Staining for neurofilament M was not altered in cuprizone fed mice. Accordingly, there was no evidence of relevant neuronal damage (*A Lower*: green = anti-phosphorylated neurofilament M antibody; blue = Hoechst dye 33258, cell nuclei). (*B*) Time course of β-APP expression (ovoids per mm^2) expressed in control mice (white bar) compared with cuprizone-fed mice (black bars).

a viscoelasticity-increasing factor supposedly generated by combined kinetics of brain maturation such as reorganization of the ECM; on the other hand, a viscoelasticity-reducing factor clearly dominated longitudinally. The latter was cuprizone-dependent: Its influence was partially reversible after discontinuing the cuprizone diet. The drop in viscoelasticity could be associated with extra-axonal reorganization, i.e., the demyelination and destruction of the ECM, but not with axonal damage. Our current data do not allow the identification of one single molecular or cellular process responsible for the observed biomechanical alterations. Nevertheless, the temporal evolution of the mechanical parameters during physiological maturation in comparison with the cuprizone-induced demyelination process reveals one important difference: During physiological maturation, the phase angle y remains constant, whereas it continuously decreases in cuprizone-treated mice. Thus, we hypothesize that the reduction of the phase angle y is exclusively assigned to demyelination. Nevertheless, there are ongoing remodeling processes of the ECM during this stage (13, 16). Unfortunately, the cohort of healthy control mice investigated in this study was too small to detect significant ECM alterations during adolescence in the conducted histological analyses. A larger trial investigating physiological ECM changes during adolescence, and the relevance of specific ECM molecules, e.g., in tenascin-receptor deficient (32, 33) as well as brevican-deficient (34) murine knock-out models, is warranted and necessary to support this hypothesis.

In a previous cross-sectional human study of 45 MS patients with recent diagnosis and mild relapsing-remitting disease course, we found a reduction of global brain viscoelasticity compared with healthy controls measured with MRE. The decrease of viscoelasticity in the corpus callosum of cuprizone mice is consistent with the data acquired in MS patients. The cuprizone model mimics particular aspects of the pathology of MS (11, 35, 36): The composition of cuprizone-induced pathology corresponds to so-called "pattern III lesions" in MS, which are characterized by oligodendroglial depletion, demyelination, and an inflammatory infiltration of activated macrophages/microglia and T lymphocytes (37). Conferring our murine cuprizone data to MS, we can assume that globally reduced cerebral viscoelasticity in patients is caused by demyelination and ECM alterations.

In conclusion, we identified structural and molecular mechanisms underlying the changes of brain parenchymal biomechanics assessed by MRE. Previously acquired human data could be reproduced in an animal model, supporting the consistency of MRE and its applicability in different species.

Materials and Methods

Detailed methods are provided in *SI Materials and Methods*. These describe mouse strains, animal handling including cuprizone diet, in vivo MRI as well as MRE procedures, and post-processing and data analysis algorithms applied. Conventional histological analyses on paraffin-embedded slices included hematoxylin and eosin (H&E) staining, Alcian blue staining, and the characterization of microglia/macrophages (anti-IBA-1), astrogliosis (anti-GFAP), T-cells (anti-CD3), myelination (anti-MBP) and the ECM proteins fibronectin (anti-fibronectin) and neurocan (anti-neurocan). Additional immunofluorescent staining on cryosections was performed for the characterization of microglia/macrophages, astroglia and axonal damage (anti-β-APP, neurofilaments H and M) as well as myelination (fluoromyelin).

ACKNOWLEDGMENTS. We thank S. Pezet and N. Nadkarni for assistance and valuable discussions.

1. Green MA, Bilston LE, Sinkus R (2008) In vivo brain viscoelastic properties measured by magnetic resonance elastography. *NMR Biomed* 21:755–764.
2. Muthupillai R, Ehman RL (1996) Magnetic resonance elastography. *Nat Med* 2: 601–603.
3. Streitberger KJ, et al. (2010) In vivo viscoelastic properties of the brain in normal pressure hydrocephalus. *NMR Biomed* 24:385–392.
4. Xu L, et al. (2007) Magnetic resonance elastography of brain tumors: preliminary results. *Acta Radiol* 48:327–330.
5. Sack I, et al. (2009) The impact of aging and gender on brain viscoelasticity. *Neuroimage* 46:652–657.
6. Wuerfel J, et al. (2010) MR-elastography reveals degradation of tissue integrity in multiple sclerosis. *Neuroimage* 49:2520–2525.
7. McDonald WI, et al. (2001) Recommended diagnostic criteria for multiple sclerosis: guidelines from the International Panel on the diagnosis of multiple sclerosis. *Ann Neurol* 50:121–127.
8. Charil A, et al. (2006) MRI and the diagnosis of multiple sclerosis: expanding the concept of "no better explanation". *Lancet Neurol* 5:841–852.
9. Matsushima GK, Morell P (2001) The neurotoxicant, cuprizone, as a model to study demyelination and remyelination in the central nervous system. *Brain Pathol* 11: 107–116.
10. Silvestroff L, et al. (2010) Cuprizone-induced demyelination in CNP:GFP transgenic mice. *J Comp Neurol* 518:2261–2283.
11. Kipp M, Clarner T, Dang J, Copray S, Beyer C (2009) The cuprizone animal model: new insights into an old story. *Acta Neuropathol* 118:723–736.
12. Rauch U (2004) Extracellular matrix components associated with remodeling processes in brain. *Cell Mol Life Sci* 61:2031–2045.
13. Squire LR (2008) *Fundamental neuroscience* (Elsevier/Academic Press, Amsterdam, Boston), 3rd Ed, pp 336–576, pp 1167–1200.
14. Baloch S, et al. (2009) Quantification of brain maturation and growth patterns in C57BL/6J mice via computational neuroanatomy of diffusion tensor images. *Cereb Cortex* 19:675–687.
15. Matthieu JM, Widmer S, Herschkowitz N (1973) Biochemical changes in mouse brain composition during myelination. *Brain Res* 55:391–402.
16. Syková E, Mazel T, Simonová Z (1998) Diffusion constraints and neuron-glia interaction during aging. *Exp Gerontol* 33:837–851.
17. Lu YB, et al. (2006) Viscoelastic properties of individual glial cells and neurons in the CNS. *Proc Natl Acad Sci USA* 103:17759–17764.
18. Lindner M, Fokuhl J, Linsmeier F, Trebst C, Stangel M (2009) Chronic toxic demyelination in the central nervous system leads to axonal damage despite remyelination. *Neurosci Lett* 453:120–125.
19. Sun SW, et al. (2006) Noninvasive detection of cuprizone induced axonal damage and demyelination in the mouse corpus callosum. *Magn Reson Med* 55:302–308.
20. Moharregh-Khiabani D, et al. (2010) Effects of fumaric acids on cuprizone induced central nervous system de- and remyelination in the mouse. *PLoS ONE* 5:e11769.
21. Koo EH, et al. (1990) Precursor of amyloid protein in Alzheimer disease undergoes fast anterograde axonal transport. *Proc Natl Acad Sci USA* 87:1561–1565.
22. Sisodia SS, Koo EH, Hoffman PN, Perry G, Price DL (1993) Identification and transport of full-length amyloid precursor proteins in rat peripheral nervous system. *J Neurosci* 13:3136–3142.
23. van Horssen J, Dijkstra CD, de Vries HE (2007) The extracellular matrix in multiple sclerosis pathology. *J Neurochem* 103:1293–1301.
24. Kwok JC, Dick G, Wang D, Fawcett JW (2011) Extracellular matrix and perineuronal nets in CNS repair. *Dev Neurobiol* 71:1073–1089.
25. Sobel RA, Mitchell ME (1989) Fibronectin in multiple sclerosis lesions. *Am J Pathol* 135: 161–168.
26. Bonneh-Barkay D, Wiley CA (2009) Brain extracellular matrix in neurodegeneration. *Brain Pathol* 19:573–585.
27. Stephens EH, Grande-Allen KJ (2007) Age-related changes in collagen synthesis and turnover in porcine heart valves. *J Heart Valve Dis* 16:672–682.
28. Huwart L, van Beers BE (2008) MR elastography. *Gastroenterol Clin Biol* 32(6, Suppl 1): 68–72.
29. Salameh N, et al. (2009) Early detection of steatohepatitis in fatty rat liver by using MR elastography. *Radiology* 253:90–97.
30. Remington LT, Babcock AA, Zehntner SP, Owens T (2007) Microglial recruitment, activation, and proliferation in response to primary demyelination. *Am J Pathol* 170: 1713–1724.
31. McMahon EJ, Suzuki K, Matsushima GK (2002) Peripheral macrophage recruitment in cuprizone-induced CNS demyelination despite an intact blood-brain barrier. *J Neuroimmunol* 130:32–45.
32. Garcion E, Faissner A, ffrench-Constant C (2001) Knockout mice reveal a contribution of the extracellular matrix molecule tenascin-C to neural precursor proliferation and migration. *Development* 128:2485–2496.
33. Brückner G, et al. (2000) Postnatal development of perineuronal nets in wild-type mice and in a mutant deficient in tenascin-R. *J Comp Neurol* 428:616–629.
34. Brakebusch C, et al. (2002) Brevican-deficient mice display impaired hippocampal CA1 long-term potentiation but show no obvious deficits in learning and memory. *Mol Cell Biol* 22:7417–7427.
35. Torkildsen O, Brunborg LA, Myhr KM, Bø L (2008) The cuprizone model for demyelination. *Acta Neurol Scand Suppl* 188:72–76.
36. Denic A, et al. (2011) The relevance of animal models in multiple sclerosis research. *Pathophysiology* 18:21–29.
37. Lucchinetti C, et al. (2000) Heterogeneity of multiple sclerosis lesions: implications for the pathogenesis of demyelination. *Ann Neurol* 47:707–717.

Supporting Information

Schregel et al. 10.1073/pnas.1200151109

SI Materials and Methods

Animals and Cuprizone Model. Female C57BL/6 mice, 5–6 wk old, were purchased from Harlan Laboratories. They were housed in groups of four animals per cage in a climate-controlled room and offered food and water ad libitum.

Two groups of each 10 animals were fed 0.2% cuprizone [oxalic acid bis (cyclo-hexylidenehydrazide)] (SAFE) mixed into normal pellet chow to induce demyelination. One group received the cuprizone diet for a period of 12 wk to evoke chronic demyelination. The other group returned to nutrition with normal pellet chow after 9 wk to study acute demyelination and remyelination subsequently (1). A third group of 10 age and sex-matched mice received continuously regular rodent nutrition and served as control group. All treated mice were observed for clinical symptoms daily.

Magnetic Resonance Imaging and Magnetic Resonance Elastography. Cerebral magnetic resonance imaging (MRI) and magnetic resonance elastography (MRE) were performed on a 7 Tesla rodent MRI scanner (Pharmascan, Bruker BioSpin). Six animals of each group were examined every 3 wk. For imaging, mice were initially anesthetized with 3% (vol/vol) Isoflurane (Aerrane, Baxter) in 100% O_2. For maintenance of anesthesia, the animal received 1–1.5% isoflurane in 100% O_2 via facemask. Mice were placed on a heating mattress to keep up body temperature during scanning. Respiration and temperature were monitored (SA Instruments).

After standard calibration, piloting and shimming, axial fat-suppressed T2-weighted (RARE; TE/TR: 66/2,213 ms, 0.60 mm slice thickness, matrix 128 × 128, field of view (FOV) 1.92 cm, 24 averages, 8 slices) and full 3D-MR-Elastography (SE sequence; TE 27 ms, TR 1,001 ms, 0.3-mm slice thickness, matrix 64 × 64, FOV 1.92 cm, 2 averages, 10 slices) images were acquired covering the same volume. Slices were positioned parallel to the most occipital tip of the olfactory bulb and covered the entire corpus callosum. For MRE, longitudinal mechanical waves at 1,000 Hz were mechanically transmitted into the mouse brain. The animal lay in supine position with its head fixed via a specially designed basket to a small vibrating piston that was coupled to a rod protruding outside the MRI. Mechanical vibrations produced by an actuator were transmitted via this rod into the brain.

Acquired MRE data were reconstructed according to published algorithms (2, 3). ROIs covering the corpus callosum were defined on anatomical images and copied to the maps of reconstructed mechanical parameters providing mean values and SDs (Fig. 1). Results are presented in terms of absolute values of the complex-valued shear modulus [i.e., $|G^*| = \mathrm{sqrt}(Gd^2 + Gl^2)$] denoted as viscoelasticity, and the phase angle y [i.e., $2/\pi * \mathrm{atan}(Gl/Gd)$], with Gd the dynamic modulus and Gl the loss modulus. Viscoelasticity expresses whether the mechanical shear parameters are elevated or not, and y informs about whether a given material behaves solid-like ($y = 0$) or liquid-like ($y = 0.5$). T2-signal intensity ratio of the corpus callosum was analyzed on anatomical T2-weighted images using open source Osirix Imaging Software (Osirix v3.9.2 32-bit; http://www.osirix-viewer.com). Three independent ROIs were positioned covering the lateral and medial corpus callosum. Two control ROIs were bilaterally positioned within the thalamus in the same MR slice. The analysis was accomplished twice in two adjacent MR slices. For the calculation of the T2 mean intensity ratio of the corpus callosum, a quotient was determined dividing the average intensity of the ROIs within the corpus callosum by the average intensity of the ROIs within the thalamus.

Statistical analysis was performed with GraphPad Prism (version 4.00 for Windows, GraphPad Software). For MRI and MRE data Bonferroni-corrected one- or two-way ANOVA were conducted and classified as significant when P value was < 0.025. The value of α had to be corrected due to double testing.

Histology. After each scanning period, two to three animals per group were killed for histological analysis. Each mouse was anesthetized with pentobarbital sodium (60 mg/kg, Céva Santé Animale) injected intraperitoneally. In the following, the animal was perfused through the heart with 100 mL of saline followed by 4% paraformaldehyde in 0.1 M PBS. The brains were removed and postfixed in 4% (wt/vol) paraformaldeyde overnight at 4 °C, then transferred in 30% (wt/vol) sucrose solution (30% sucrose in 0.2 M PBS) for dehydratation. One half of the brains were embedded in paraffin. The remaining brains were embedded into tissue freezing medium (OCT compound Tissue-Tek, Sakura Finetek Europe), frozen in liquid nitrogen, and stored at −80 °C.

The paraffin-embedded tissues were sectioned into 3-μm-thick slices using a microtome (Hn40, Leica Microsystems) and stained by standard hematoxylin and eosin (H&E) and Alcian blue staining.

Conventional immunohistochemical stainings were performed with paraffin-embedded slices using anti-IBA-1-antibody (1:1,000, rabbit-anti-iba-1-antibody, WAKO Chemicals) for characterization of microglia/macrophages, anti-GFAP-antibody (1:500, polyclonal rabbit anti-glial-fibrillary-acidic-protein antibody, Dako Deutschland) for astrogliosis, anti-CD3-antibody (1:150; Labvision, Thermo Fisher Scientific) for the detection of T-cells and anti-MBP-antibody (1:100, polyclonal rabbit myelin basic protein antibody, Abcam) for myelination. The stainings were realized using the Bond Automated Immunohistochemistry & In-Situ Hybridization System (A. Menarini Diagnostics).

Immunohistochemical stainings for extracellular matrix proteins were accomplished using anti-neurocan-antibody (1:1,000, mouse-monoclonal anti-Neurocan antibody) and anti-fibronectin-antibody (1:400, rabbit polyclonal anti-Fibronectin antibody, both Abcam). For antigen-retrieval, 3-μm axial paraffin-embedded sections were heated at 120 °C in citrate buffer (pH 6) for 7 min. They were incubated with the above named primary antibodies for 1 h and with the secondary antibodies for 20 min and 30 min, respectively (for neurocan staining: biotinylated goat-anti-mouse, ready to use, Zytomed; for fibronectin staining: biotinylated donkey-anti-rabbit 1:2,000, Dianova). In the following, the sections were incubated in Streptavidin-HRS (ready to use, Zytomed) for 20 min and in 3-Amino-9-Ethylcarbazole (AEC, Invitrogen) for another 15 min. Nuclei were counterstained with hematoxylin.

Additionally, immunofluorescent stainings were performed using the above described anti-IBA-1- and anti-GFAP-antibodies. Briefly, 10 μm axial cryosections (Kryostat 1720, Leica Microsystems) were preincubated with 4% (vol/vol) normal goat serum for 1 h to block nonspecific bindings. Sections were subsequently incubated with the primary antibody in 0,1 M PBS overnight at 4 °C and then with the secondary antibody (1:500, goat anti-rabbit IgG, AlexaFluor 488, Invitrogen, Cergy-Pontoise, France) for 1 h at 4 °C. Slices were counterstained with fluoromyelin (1:50, Invitrogen) to visualize myelin and Hoechst dye 33258 (1:1,000, Invitrogen) to depict cell nuclei. Analysis of axonal damage has been performed by costaining with anti-APP (1:400, rabbit polyclonal anti-human amyloid precursor protein antibody, AbD Serotec), anti-SMI-31R (1:2,000 dilution, mouse monoclonal anti-phosphorylated neurofilament H and M antibody, Covance), anti-SMI-34R (1:2,000 dilution, mouse mono-

clonal anti-phosphorylated neurofilament H and M antibody, Covance) in 2.5% (vol/vol) normal goat serum, 0.5% BSA 0.1%, Triton X100, overnight at 4 °C, followed by staining for 1 h at room temperature with goat secondary antibody 1:500 dilution conjugated with AlexaFluor 546 or AlexaFluor 488 (Molecular Probes, Invitrogen).

Sections were examined with light and epifluorescence microscopy (Leica, Carl Zeiss) and digitally photographed and processed using AxioVision (Carl Zeiss MicroImaging). Two independent investigators performed the histological analyses after agreement on a semiquantative scoring system respectively for the evaluation of myelination, extracellular matrix proteins, astrogliosis, and presence of microglia/macrophages or T lymphocytes. For each of these parameters, a score was introduced rating from 4 to 0. (Score for myelination: 4 = normal myelination, 3 = slightly reduced myelination, 2 = largely impaired myelination, 1 = minor myelination, 0 = no myelin; Score for astrogliosis or the presence of macrophages/microglia, respectively: 4 = massive, 3 = pronounced, 2 = moderate, 1 = minor, 0 = none; Score for extracellular matrix alterations: 3 = largely impaired extracellular matrix structure with severe degradation, 2 = moderate degradation, 1 = slightly altered extracellular matrix and 0 = normal; Score for fibronectin and Alcian blue: 3 = intense deposition, 2 = moderate deposition, 1 = sparse deposition, 0 = none). Quantification of T-cell numbers was conducted by manual counting of clearly visible CD3-positive cells in the corpus callosum in six subsequent slices.

Statistical analyses of histological data were accomplished using GraphPad Prism. Healthy controls were pooled as they did not show differing values at all time points. Cuprizone mice were compared with pooled controls at every time point conducting conventional unpaired *t* tests. Consequently, α was adjusted due to multiple testing and had results were classified as significant when *P* value was < 0.01.

1. Kipp M, Clarner T, Dang J, Copray S, Beyer C (2009) The cuprizone animal model: new insights into an old story. *Acta Neuropathol* 118:723–736.
2. Green MA, Bilston LE, Sinkus R (2008) In vivo brain viscoelastic properties measured by magnetic resonance elastography. *NMR Biomed* 21:755–764.
3. Sinkus R, et al. (2007) MR elastography of breast lesions: understanding the solid/liquid duality can improve the specificity of contrast-enhanced MR mammography. *Magn Reson Med* 58:1135–1144.

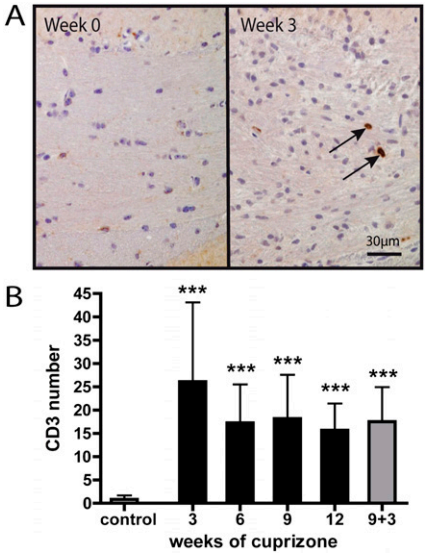

Fig. S1. The presence of T lymphocytes was assessed on immunohistochemical stainings using anti-CD3-antibodies. (*A*) In healthy controls (HC; *Left*) only few T-cells were detectable, whereas cuprizone-treated animals (CUP; *Right*) showed elevated numbers of CD3-positive cells (arrows). (*B*) Quantitative analysis of the longitudinal T-cell count in the corpus callosum. Only few T cells were found in HC (white bar). In CUP (black bars), an early immigration of a small number of T lymphocytes into the corpus callosum was observed. The number of T cells was most pronounced after 3 wk of cuprizone diet. ***$P < 0.0001$; treated mice compared with controls in an unpaired *t* test at every time point (in consequence, α was lowered and results were classified significant when *P* value was $<$ 0.01). SD by whiskers.

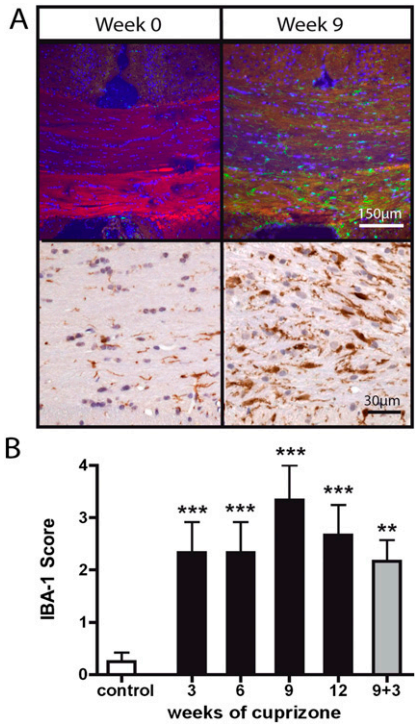

Fig. S2. Presence of activated microglia/macrophage (aM/M) was determined by immunohistochemical staining for IBA-1. (*A*) After 9 wk of cuprizone feeding, the density of aM/M was largely elevated (image top right; green = IBA-1, aM/M; blue = Hoechst 33258, cell nuclei; red = fluoromyelin) compared with healthy mice (HC) at week 0 (*Upper Left*). (*B*) Semiquantitative analysis of the presence of aM/M in the corpus callosum assessed with a score rating from 0 (none) to 4 (massive infiltration). HC (white bar) were pooled. In treated animals (CUP; black bars), a significantly increased number of stained cells was detectable starting at week 3, and peaked at week 9, and declined after 12 wk of cuprizone feeding. $^{**}P < 0.001$, $^{***}P < 0.0001$; CUP compared with HC in an unpaired *t* test at every time point (in consequence, α was lowered and results were classified as significant when *P* value was < 0.01). SD by whiskers.